A general framework to quantify the effect of restricted diffusion on the NMR signal with applications to double pulsed field gradient NMR experiments

Evren Özarslan,[1,a)] Noam Shemesh,[2] and Peter J. Basser[1]
[1]*Section on Tissue Biophysics and Biomimetics, NICHD, National Institutes of Health, 13 South Drive, Bethesda, Maryland 20892, USA*
[2]*School of Chemistry, The Raymond and Beverly Sackler Faculty of Exact Sciences, Tel Aviv University, 69978 Ramat Aviv, Israel*

(Received 8 December 2008; accepted 27 January 2009; published online 9 March 2009)

Based on a description introduced by Robertson, Grebenkov recently introduced a powerful formalism to represent the diffusion-attenuated NMR signal for simple pore geometries such as slabs, cylinders, and spheres analytically. In this work, we extend this multiple correlation function formalism by allowing for possible variations in the direction of the magnetic field gradient waveform. This extension is necessary, for example, to incorporate the effects of imaging gradients in diffusion-weighted NMR imaging scans and in characterizing anisotropy at different length scales via double pulsed field gradient (PFG) experiments. In cylindrical and spherical pores, respectively, two- and three-dimensional vector operators are employed whose form is deduced from Grebenkov's results via elementary operator algebra for the case of cylinders and the Wigner–Eckart theorem for the case of spheres. The theory was validated by comparison with known findings and with experimental double-PFG data obtained from water-filled microcapillaries. © *2009 American Institute of Physics*. [DOI: 10.1063/1.3082078]

I. INTRODUCTION

The problem of restricted diffusion in the presence of magnetic field inhomogeneities has attracted widespread interest. This is because the nuclear magnetic resonance (NMR) experiments can be sensitized to diffusional motion of spin-bearing molecules making it feasible to obtain structural information from porous materials, colloidal systems, and biological tissue noninvasively. Application of a well-controlled sequence of magnetic field inhomogeneities, hereafter referred to as a gradient waveform, enables different features of the specimen's microstructure to be revealed.

For example, the incorporation of a pair of linear gradient pulses around the 180° radiofrequency (rf) pulse in a Hahn spin-echo experiment[1] has enabled the recovery of tremendous amounts of information. A special case is the pulsed field gradient (PFG) experiment[2] that uses two infinitesimally short gradient pulses. This simplifies the problem theoretically since Green's function (propagator) based methods can be used readily to find expressions for the NMR signal intensity. Such an experiment, however, is not feasible for many problems of interest where long duration pulses need to be applied. Moreover, information not available from the two-pulse experiments can be obtained when more sophisticated gradient waveforms are used. Therefore, it is desirable to develop a theory that applies to arbitrary gradient waveforms.

One such approach involved discretizing a general gradient waveform and approximating it by a train of impulses.[3] In this case, diffusion can be thought to be taking place in the absence of diffusion gradients and expressions for NMR signal intensity can be obtained by using a series of propagators linking the time points at which consecutive impulses are applied. A reformulation of this approach yielded the signal intensities as the product of matrices.[4–7] Well-controlled experiments on fused cylindrical microcapillaries validated the accuracy of the technique.[8,9]

An alternative approach to understanding the effect of restricted diffusion is to treat a general gradient waveform as a piecewise-constant function.[10,11] Such a sequence is illustrated in Fig. 1(a). Treating the effect of diffusion in piecewise-constant gradients is historically important because in the presence of a constant gradient, the spin-echo signal is effectively attenuated via a bipolar pulse, where each lobe of the bipolar pulse occupies half the echo time.[12] A novel formalism to predict the resulting spin-echo signal was introduced by Robertson,[13] who applied quantum mechanical techniques to the problem of magnetization evolution when spins are trapped between two parallel infinite plates. Another important application of piecewise-constant gradients naturally arises in the Carr–Purcell–Meiboom–Gill experiment[12,14] that was studied extensively in Refs. 15 and 16. Recently, Grebenkov refined the idea of approximating a general waveform with a piecewise-constant function, extending Robertson's description to cylindrical and spherical volumes and layers, which has led to a powerful multiple correlation function (MCF) method that yields simple analytical expressions for the NMR echo intensity.[17–19] These expressions are given by a product of temporal evolution operators, represented by matrix exponentials,[13] where the

[a)]Electronic mail: evren@helix.nih.gov.

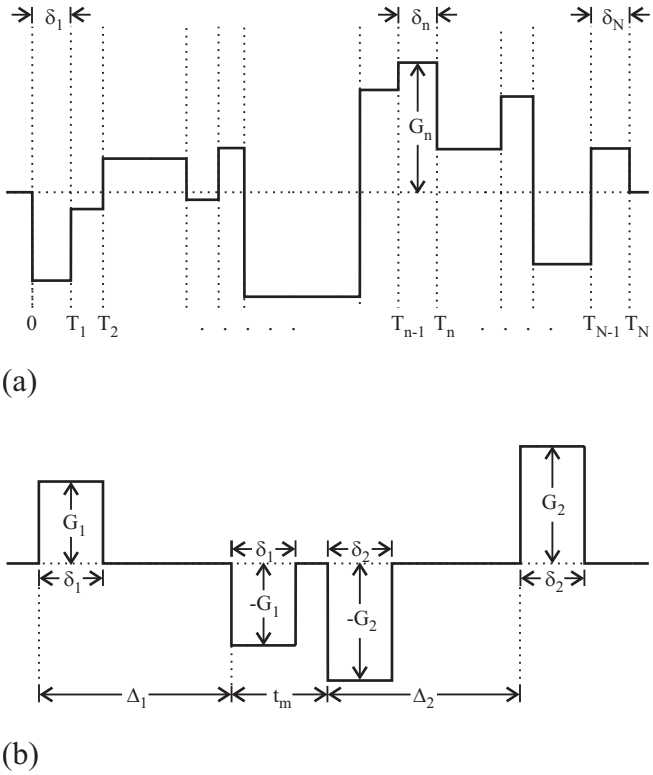

FIG. 1. (a) A general piecewise-constant gradient waveform is shown in the top row. It is assumed that all rf pulses are taken into consideration so that the waveform drawn is the effective gradient profile (Ref. 28). There are a total of N intervals. During the nth interval, the gradient $\mathbf{G}_n$ is applied for a duration δ_n between the time points T_{n-1} and T_n. (b) The technique developed is applied to the double-PFG pulse sequence whose effective gradient waveform is depicted at the bottom. The intervals Δ_1 and Δ_2 denote the separation between the two pulses of each PFG block employing gradients of durations δ_1 and δ_2, respectively. The two PFG blocks are separated from each other by the mixing time t_m.

elements of the matrices are tabulated in Refs. 17 and 18 for the simple geometries of slabs, cylinders, and spheres.

The MCF technique, in its current form, employs a simplifying assumption regarding the orientation of the gradients. Specifically, in the case of a cylindrical pore whose orientation defines the z axis, the gradients are assumed to be along the x direction; in the case of the spherical pore, they are assumed to be along the z direction. When these assumptions are employed, the MCF technique cannot accommodate variations in the gradient orientation within the pulse sequence.

There are at least two important applications in which one has to incorporate variations in gradient directions. First, in MR image acquisitions, gradients are applied along all three directions to spatially encode the collected signal. Therefore, if one is interested in quantifying the effect of restricted diffusion in imaging scans or in analyzing the interaction between the imaging and diffusion sensitizing gradients, it is necessary to employ a more general theory. Second, a logical extension of single-PFG acquisitions has involved repeated application of gradient pulse pairs.[20] A realization of this pulse sequence is the double-PFG experiment [illustrated in Fig. 1(b)] in which the dependence of the signal on the angle between the two gradient vectors reflects features of restricted diffusion that can be used to obtain estimates of compartment size.[21,22] The theory in Ref. 22 provided explicit solutions for the double-PFG NMR signal intensity with arbitrary gradient timing parameters when the long wavelength assumption is satisfied, i.e., at small gradient strengths. Experiments performed on well-controlled NMR phantoms consisting of cylindrical tubes suggested that the predictions of Ref. 22 can be employed to obtain accurate estimates of small compartmental dimensions.[23]

In a different study, it was predicted that when all gradient orientations were kept parallel to each other in a multi-PFG acquisition with an even number of gradient pulse pairs, increasing the gradient strength would yield peculiar features such as zero crossings that are robust to the heterogeneity of the specimen.[7] These predictions were validated experimentally.[24] Therefore, the application of MCF generalized to handle variations in the gradient orientation can be used to build a unified theory for double-PFG experiments for completely arbitrary experimental parameters that can handle both the anisotropy induced in subcompartmental length scales and the peculiar diffraction-like effects.

In this article, we start by providing a review of the MCF approach in Sec. II. In Sec. III the MCF technique is generalized to include variations in the direction of the applied gradients. In Sec. IV the developed theory is applied to double-PFG acquisitions and validated with real data obtained from cylindrical microcapillaries.

II. A BRIEF REVIEW OF THE MCF FRAMEWORK

In this section, for completeness, we shall review the MCF approach generalizing Robertson's method. The MCF technique assumes a piecewise-constant gradient waveform as shown in Fig. 1(a). It should be noted that an arbitrary waveform can be approximated by a piecewise function, so the method provides an appropriate approximation for arbitrary gradient waveforms. The technique is based on solving the magnetization evolution equation (the Bloch–Torrey equation),[25]

$$\frac{\partial M(\mathbf{r},t)}{\partial t} = D_0 \nabla^2 M(\mathbf{r},t) - i\gamma \mathbf{G}(t)\cdot \mathbf{r} M(\mathbf{r},t), \tag{1}$$

where $M(\mathbf{r},t)$ is a complex-valued function denoting the transverse magnetization density at location $\mathbf{r}$ at time t, D_0 is the diffusion coefficient, γ is the gyromagnetic ratio, and $\mathbf{G}(t)$ is the linear magnetic field gradient waveform. In the above expression, the Larmor precession and relaxation terms are excluded as we are interested in the attenuation due solely to diffusion. The MCF method is based on the eigenspectrum of the Laplacian operator, where the kth eigenfunction, $u_k(\mathbf{r})$, satisfies the Helmholtz equation,

$$\nabla^2 u_k(\mathbf{r}) = -\frac{\lambda_k}{D_0} u_k(\mathbf{r}), \tag{2}$$

along with the Neumann boundary condition, $\hat{\mathbf{n}}\cdot\nabla u_k(\mathbf{r})|_{\mathbf{r}\in\Sigma} = 0$, where $\hat{\mathbf{n}}$ is the direction perpendicular to the boundary Σ, which is assumed to be reflective.

Note that the eigenfunctions, $u_k(\mathbf{r})$, are the same functions used in the eigenfunction expansion of the diffusion propagator whose long time asymptotic demands one of the

eigenvalues to vanish.[22] If this eigenvalue is assigned the index 0, i.e., $\lambda_0=0$, then $u_0(\mathbf{r})=V^{-1/2}$, where V denotes the pore volume.

The treatment we present here is based on Robertson's original framework and the MCF technique with minor differences in the definitions. However, we allow for the possibility that $\mathbf{G}(t)$ may change its orientation. In addition, as in Ref. 26, we employ Dirac's bra-ket notation to denote vectors in an ∞-dimensional Hilbert space as it is necessary to distinguish them from vectors in physical two- or three-dimensional space. In this notation, the transverse magnetization is denoted as

$$M(\mathbf{r},t)=\langle \mathbf{r}|M(t)\rangle, \tag{3}$$

and the eigenfunctions are given by

$$u_k(\mathbf{r})=\langle \mathbf{r}|k\rangle. \tag{4}$$

The eigenfunctions of the Laplacian operator form a complete orthonormal basis where the orthonormality condition can be expressed as

$$\int d\mathbf{r}\langle k|\mathbf{r}\rangle\langle \mathbf{r}|k'\rangle=\langle k|k'\rangle=\delta_{kk'}, \tag{5}$$

and the completeness relation is given by

$$\sum_k |k\rangle\langle k|=I, \tag{6}$$

where I is the ∞-dimensional identity operator. The index k runs over all eigenstates of the Laplacian.

Inserting the completeness relation into Eq. (3), we obtain the relation

$$\langle \mathbf{r}|M(t_n)\rangle=\sum_{k'}\langle \mathbf{r}|k'\rangle\langle k'|M(t_n)\rangle, \tag{7}$$

which is just the expansion of the magnetization in the Laplacian eigenbasis[27] with coefficients $\langle k'|M(t_n)\rangle$. The subscript n was added to stress that we are considering the nth time interval, i.e., $T_{n-1}\le t\le T_n$. Note that $\mathbf{G}$ is constant in any such interval and will be denoted by $\mathbf{G}_n$. Substituting the above form of the magnetization into Eq. (1), we obtain

$$\sum_{k'}\langle \mathbf{r}|k'\rangle\frac{\partial}{\partial t_n}\langle k'|M(t_n)\rangle=-\sum_{k'}\langle k'|M(t_n)\rangle\lambda_{k'}\langle \mathbf{r}|k'\rangle - i\gamma\mathbf{G}_n\cdot\mathbf{r}\sum_{k'}\langle \mathbf{r}|k'\rangle\langle k'|M(t_n)\rangle, \tag{8}$$

where we have also employed Eq. (2). Multiplying both sides of the above expression by $\langle k|\mathbf{r}\rangle$ and integrating over $\mathbf{r}$ leads to the expression

$$\frac{\partial}{\partial t_n}\langle k|M(t_n)\rangle=-\sum_{k'}\langle k'|M(t_n)\rangle\lambda_{k'}\delta_{kk'} - i\gamma\sum_{k'}\langle k'|M(t_n)\rangle\mathbf{G}_n\cdot\int d\mathbf{r}\langle k|\mathbf{r}\rangle\mathbf{r}\langle \mathbf{r}|k'\rangle. \tag{9}$$

It is helpful to introduce an ∞-dimensional operator, Λ, whose matrix elements are given by

$$\langle k|\Lambda|k'\rangle=\lambda_{k'}\delta_{kk'}. \tag{10}$$

Furthermore, we introduce a vector operator, $\mathbf{A}$, through the expression

$$\langle k|\mathbf{A}|k'\rangle=\int d\mathbf{r}\langle k|\mathbf{r}\rangle\mathbf{r}\langle \mathbf{r}|k'\rangle. \tag{11}$$

Employing these two definitions, the evolution equation, Eq. (9), becomes

$$\frac{\partial}{\partial t_n}|M(t_n)\rangle=-(\Lambda+i\gamma\mathbf{G}_n\cdot\mathbf{A})|M(t_n)\rangle, \tag{12}$$

which is readily solved to yield the expression

$$|M(t_n)\rangle=e^{-(\Lambda+i\gamma\mathbf{G}_n\cdot\mathbf{A})(t_n-T_{n-1})}|M(T_{n-1})\rangle \tag{13}$$

describing the time evolution of the magnetization ket within the nth interval given its state at time T_{n-1}.

Since in the conventional depiction of the pulse sequences, the pulses applied later are drawn to the right of the earlier pulses, it proves convenient to express the evolution of the magnetization bra. Such an expression, obtained by taking the Hermitian conjugate of the preceding expression, is given by

$$\langle M(t_n)|=\langle M(T_{n-1})|e^{-(\Lambda-i\gamma\mathbf{G}_n\cdot\mathbf{A}^\dagger)(t_n-T_{n-1})}. \tag{14}$$

With the particular choice of $t_n=T_n$ and using the definitions $\delta_n=T_n-T_{n-1}$ and $\mathbf{q}_n=(2\pi)^{-1}\gamma\delta_n\mathbf{G}_n$, we obtain the relation

$$\langle M(T_n)|=\langle M(T_{n-1})|e^{-\Lambda\delta_n+i2\pi\mathbf{q}_n\cdot\mathbf{A}^\dagger}. \tag{15}$$

The recursive character of this equation can be exploited to extend it in both temporal directions to cover the time axis from $t=0$ to $t=T_N$:

$$\langle M(T_N)|=\langle M(0)|\prod_{n=1}^{N}e^{-\Lambda\delta_n+i2\pi\mathbf{q}_n\cdot\mathbf{A}^\dagger}. \tag{16}$$

Since magnetization density at the start of the pulse sequence is a constant across the pore space, it can be assigned to be the reciprocal of the pore volume V; this ensures that in the absence of any gradients, the signal is unity. Therefore,

$$\langle \mathbf{r}|M(0)\rangle=\frac{1}{V}=\sum_k\langle \mathbf{r}|k\rangle\langle k|M(0)\rangle. \tag{17}$$

This expression dictates $\langle \mathbf{r}|k\rangle$ to be spatially independent. Consequently, all elements of the initial magnetization vector except at $k=0$ should vanish. This observation, along with the previously discussed expression $\langle \mathbf{r}|0\rangle=V^{-1/2}$, determines the initial magnetization bra to be

$$\langle M(0)| = V^{-1/2}\langle 0|. \tag{18}$$

The detected MR signal attenuation is just the integral of the final magnetization density over the pore space, i.e.,

$$E = \int d\mathbf{r}\langle \mathbf{r}|M(T_N)\rangle = \sum_k \langle k|M(T_N)\rangle \int d\mathbf{r}\langle \mathbf{r}|k\rangle. \tag{19}$$

The integral in the last expression can be evaluated to be $V^{1/2}\langle 0|k\rangle$ by multiplying the integrand by $1 = V^{1/2}\langle 0|\mathbf{r}\rangle$ and using the orthonormality of the eigenfunctions. Therefore, the NMR signal attenuation is given simply by

$$E = V^{1/2}\langle 0|M(T_N)\rangle = V^{1/2}\langle M(T_N)|0\rangle^*. \tag{20}$$

Inserting Eq. (18) into Eq. (16) and the resulting expression into Eq. (20), we obtain the NMR signal attenuation from a piecewise-constant gradient waveform to be

$$E = \langle 0|\prod_{n=1}^{N} e^{-\Lambda\delta_n + i2\pi\mathbf{q}_n\cdot\mathbf{A}^\dagger}|0\rangle^*. \tag{21}$$

III. GENERALIZATION OF THE MCF TECHNIQUE

Equation (21) suggests that the NMR signal attenuation can be obtained conveniently from the operators Λ and $\mathbf{A}$. In the case of the slab geometry, $\mathbf{A}$ is a scalar operator, which can be represented by a single ∞-dimensional matrix. When the gradient is applied at an angle oblique to the surface of the parallel plates, separation of variables can be employed to decompose the gradient vector into components parallel and perpendicular to the plates, so the signal can be written as the product of the contributions from restricted and free diffusions. The free diffusion expression for arbitrary gradient waveforms can be found in Refs. 22 and 28. The contribution to the signal attenuation from restricted diffusion can be obtained from Eq. (21), where the operators Λ and $\mathbf{A}$ are ∞-dimensional matrices whose elements are derived in Ref. 19 and tabulated in Ref. 18. Therefore, we do not discuss the parallel plate geometry any further.

Reference 18 provides the matrix elements for the cylindrical and spherical pores as well. However, supposing that the symmetry axis of the cylinder is along the z direction, the expressions in Ref. 18 assume that the gradient vectors are consistently along the x and z directions throughout the pulse sequence in the case of cylinders and spheres, respectively. To employ the MCF technique in more general pulse sequences, other components of the vector operator $\mathbf{A}$ must be determined. In this section, we derive the relevant expressions effectively by rotating the vector operator to find its other components.

A. The cylindrical pore

In this section we shall tackle the problem of the cylindrical pore. Any component of the gradient along the cylinder's axis can be handled in a way similar to the scheme described above for the case of oblique gradients in the parallel plate geometry. The interesting part of the problem involves the components of the gradient vector lying in the transverse plane, which is taken to be the xy plane. For this geometry, the vector operator $\mathbf{A}$ has two components, i.e.,

$$\mathbf{A} = \begin{pmatrix} X \\ Y \end{pmatrix}, \tag{22}$$

where X and Y are ∞-dimensional matrices. As provided in Ref. 18, the elements of the operators Λ and X are given by

$$\Lambda_{km,k'm'} = \delta_{kk'}\delta_{mm'}\frac{\alpha_{km}^2 D_0}{r_0^2} \tag{23}$$

and

$$X_{km,k'm'} = r_0\delta_{m,m'\pm 1}(1+\delta_{m,0}+\delta_{m',0})^{1/2} \times \beta_{km}\beta_{k'm'}\frac{\alpha_{km}^2+\alpha_{k'm'}^2-2mm'}{(\alpha_{km}^2-\alpha_{k'm'}^2)^2}, \tag{24}$$

where r_0 is the radius of the cylinder and α_{km} is the kth zero of the derivative of the mth order Bessel function, i.e., it satisfies the equation $J_m'(\alpha_{km})=0$. Finally, β_{km} is given by

$$\beta_{km} = \begin{cases} 1 & \text{if } k=m=0 \\ \dfrac{\alpha_{km}}{(\alpha_{km}^2-m^2)^{1/2}} & \text{otherwise.} \end{cases} \tag{25}$$

The eigenfunctions for the cylindrical geometry have radial and angular parts. Since we are interested in rotations, we consider only the angular part of the eigenfunction, which is given by

$$\langle \phi|m\rangle = (2\pi)^{-1/2}e^{im\phi}, \tag{26}$$

where ϕ is the polar angle of the cylindrical coordinates and m is any integer. Let $L=d/d\phi$ denote the generator of rotations in two-dimensional space. The matrix elements of L in this basis are given by

$$\langle m|L|m'\rangle = \frac{1}{2\pi}\int_0^{2\pi} d\phi e^{-im\phi}\frac{d}{d\phi}e^{im'\phi} = im\delta_{mm'}. \tag{27}$$

Therefore, L is diagonal. Note that Eq. (10) suggests that Λ is diagonal as well. Consequently, Λ commutes with L, hence is invariant under rotations.

The X matrix, however, is not invariant under rotations. The Y matrix can be obtained from X via a 90° rotation, i.e.,

$$\begin{aligned} Y &= \exp\left(\frac{\pi}{2}L\right)X\exp\left(-\frac{\pi}{2}L\right) \\ &= X + \frac{\pi}{2}\frac{1}{1!}[L,X] + \left(\frac{\pi}{2}\right)^2\frac{1}{2!}[L,[L,X]] \\ &\quad + \left(\frac{\pi}{2}\right)^3\frac{1}{3!}[L,[L,[L,X]]] + \cdots, \end{aligned} \tag{28}$$

where in the last step we employed an identity that follows from the Baker–Campbell–Hausdorff formula.

The matrix elements of the commutator of X with L are given from Eqs. (24) and (27) to be

$$\langle km|[L,X]|k'm'\rangle = i(m-m')\langle km|X|k'm'\rangle. \tag{29}$$

Therefore, each application of the commutator adds another factor of $i(m-m')$. This observation leads to the realization that the series in Eq. (28) is a Taylor series, where the $(km,k'm')$th element of the operator Y evaluates to $e^{i\pi/2(m-m')}\langle km|X|k'm'\rangle$. Note that since the only nonzero elements of X are obtained when $m=m'\pm 1$, this finding suggests that the matrix elements of the operator Y are essentially the same as those of X, the only differences being a global multiplication by i and a sign change in the elements right above the diagonal elements, i.e.,

$$Y_{km,k'm'} = ir_0(\delta_{m,m'+1} - \delta_{m,m'-1})(1+\delta_{m,0}+\delta_{m',0})^{1/2} \times \beta_{km}\beta_{k'm'}\frac{\alpha_{km}^2+\alpha_{k'm'}^2-2mm'}{(\alpha_{km}^2-\alpha_{k'm'}^2)^2}. \tag{30}$$

B. The spherical pore

In the case of the spherical pore, the problem is three dimensional, and the vector operator $\mathbf{A}$ has three components, i.e.,

$$\mathbf{A} = \begin{pmatrix} X \\ Y \\ Z \end{pmatrix}. \tag{31}$$

Reference 18 provides the relevant matrix elements for a $\mathcal{B}$ operator, which are given by

$$\mathcal{B}_{kl,k'l'} = R_0\delta_{l,l'\pm 1}\frac{l+l'+1}{(2l+1)(2l'+1)} \times \beta_{kl}\beta_{k'l'}\frac{\alpha_{kl}^2+\alpha_{k'l'}^2-l(l'+1)-l'(l+1)+1}{(\alpha_{kl}^2-\alpha_{k'l'}^2)^2}, \tag{32}$$

where R_0 is the radius of the sphere and α_{kl} is the kth zero of the derivative of the lth order spherical Bessel function, i.e., it satisfies the equation $j_l'(\alpha_{kl})=0$. Finally, β_{kl} is given by

$$\beta_{kl} = \begin{cases} \sqrt{\frac{3}{2}} & \text{if } k=l=0 \\ \alpha_{kl}\left(\frac{2l+1}{\alpha_{kl}^2-l(l+1)}\right)^{1/2} & \text{otherwise.} \end{cases} \tag{33}$$

Note that these derivations are based on the form of the eigenfunction whose angular part is

$$\langle\theta|l\rangle = \sqrt{\frac{2l+1}{2}}P_l(\cos\theta), \tag{34}$$

where $P_l(\cdot)$ is the lth order Legendre polynomial. Clearly, this is a "reduced" version of the real eigenfunction, which should depend on the azimuthal angle ϕ as well. Since the gradients were assumed to be applied along the z direction in Ref. 18, the result was independent of the azimuthal angle and the associated state index m. However, this is no longer the case if we allow the gradients to be applied along other directions. Therefore, we need to employ the full version of the eigenfunctions whose angular part is given by the spherical harmonics, i.e.,

$$\langle\theta,\phi|lm\rangle = Y_{lm}(\theta,\phi). \tag{35}$$

If these eigenfunctions were employed, the $m=m'=0$ component of the Z matrix would be the same as $\mathcal{B}$ since $\langle\theta,\phi|l0\rangle=\langle\theta|l\rangle$. Moreover, it is straightforward to prove that Z is m diagonal. In this basis, the components of the matrix Λ are given simply by

$$\langle k'l'm'|\Lambda|klm\rangle = \langle k'|k\rangle\langle l'|l\rangle\langle m'|m\rangle\frac{\alpha_{kl}^2 D_0}{R_0^2}. \tag{36}$$

It may be possible to follow the same scheme as in the case of a cylindrical pore to find the matrix elements of the components of the vector operator $\mathbf{A}$. However, the Wigner–Eckart theorem provides an elegant and simpler way of obtaining all components. It states that the matrix elements of an irreducible spherical tensor operator of rank K, denoted by T_K^Q $(Q=-K,-K+1,\ldots,K-1,K)$, can be written as[29]

$$\langle k'l'm'|T_K^Q|klm\rangle = \langle lKmQ|lKl'm'\rangle\langle k'l'||T_K||kl\rangle, \tag{37}$$

where the first factor on the right hand side is a Clebsch–Gordan coefficient, and $\langle k'l'||T_K||kl\rangle$ is a reduced matrix element of the irreducible spherical tensor operator T_K, which is independent of the indices m, m', and Q.

Note that since $\mathbf{A}$ is a vector operator, $K=1$. To apply this theorem, we need to transform the vector operator $\mathbf{A}$ into its irreducible spherical tensor operator form, which is accomplished through the well-known relations

$$T_1^{+1} = -\frac{X+iY}{\sqrt{2}}, \tag{38a}$$

$$T_1^0 = Z, \tag{38b}$$

$$T_1^{-1} = \frac{X-iY}{\sqrt{2}}. \tag{38c}$$

We first apply the Wigner–Eckart theorem for the case $Q=0$. In this case, the selection rules associated with the corresponding Clebsch–Gordan coefficient ensure that $m=m'$ and $l-1\le l'\le l+1$.

We first consider the case $l'=l$ along with $m'=m$. The Wigner–Eckart theorem implies the relation

$$\langle k'lm|T_1^0|klm\rangle = \frac{m}{\sqrt{l(l+1)}}\langle k'l||T_1||kl\rangle. \tag{39}$$

However, the diagonal matrix elements of $T_1^0=Z$ are proportional to

$$\langle k'lm|T_1^0|klm\rangle \propto \int_0^{2\pi}d\phi\int_0^{\pi}d\theta\sin\theta\cos\theta Y_{lm}(\theta,\phi)^* Y_{lm}(\theta,\phi) = \frac{2l+1}{2}\frac{(l-m)!}{(l+m)!}\int_{-1}^{1}d\mu\mu P_{lm}(\mu)^2, \tag{40}$$

where $P_{lm}(\cdot)$ denotes the associated Legendre functions. The above expression vanishes because the integrand in the last

integral is an odd function of μ. Therefore, Eq. (39) implies

$$\langle k'l||T_1||kl\rangle = 0. \tag{41}$$

Next, we consider that $l'=l+1$ along with $m'=m=0$. In this case, the Wigner–Eckart theorem states that

$$\langle k'(l+1)|\mathcal{B}|kl\rangle = \langle k'(l+1)0|T_1^0|kl0\rangle = \langle l100|l1(l+1)0\rangle\langle k'(l+1)||T_1||kl\rangle. \tag{42}$$

Plugging in the value for the Clebsch–Gordan coefficient, we obtain the reduced matrix element to be

$$\langle k'(l+1)||T_1||kl\rangle = \sqrt{\frac{2l+1}{l+1}}\langle k'(l+1)|\mathcal{B}|kl\rangle. \tag{43}$$

Repeating the same analysis for the case $l'=l-1$ along with $m'=m=0$, we obtain the remaining nonzero reduced matrix elements given by

$$\langle k'(l-1)||T_1||kl\rangle = -\sqrt{\frac{2l+1}{l}}\langle k'(l-1)|\mathcal{B}|kl\rangle. \tag{44}$$

Having the reduced matrix elements, we can now employ the Wigner–Eckart theorem repeatedly to find all components of the irreducible spherical vector operator, T_1^Q. Straightforward algebra reveals these matrix elements to be

$$\langle k'(l+1)m|T_1^0|klm\rangle = \frac{\sqrt{(l+1)^2-m^2}}{l+1}\langle k'(l+1)|\mathcal{B}|kl\rangle, \tag{45a}$$

$$\langle k'(l-1)m|T_1^0|klm\rangle = \frac{\sqrt{l^2-m^2}}{l}\langle k'(l-1)|\mathcal{B}|kl\rangle, \tag{45b}$$

$$\langle k'(l+1)(m+1)|T_1^{+1}|klm\rangle = \sqrt{\frac{(l+m+1)(l+m+2)}{2}}\frac{1}{l+1}\langle k'(l+1)|\mathcal{B}|kl\rangle, \tag{45c}$$

$$\langle k'(l-1)(m+1)|T_1^{+1}|klm\rangle = -\sqrt{\frac{(l-m-1)(l-m)}{2}}\frac{1}{l}\langle k'(l-1)|\mathcal{B}|kl\rangle, \tag{45d}$$

$$\langle k'(l+1)(m-1)|T_1^{-1}|klm\rangle = \sqrt{\frac{(l-m+1)(l-m+2)}{2}}\frac{1}{l+1}\langle k'(l+1)|\mathcal{B}|kl\rangle, \tag{45e}$$

$$\langle k'(l-1)(m-1)|T_1^{-1}|klm\rangle = -\sqrt{\frac{(l+m-1)(l+m)}{2}}\frac{1}{l}\langle k'(l-1)|\mathcal{B}|kl\rangle, \tag{45f}$$

where all other matrix elements vanish as a result of the selection rules ($m'=m+Q$, and $|l'-l|\leq 1$) dictated by the relevant Clebsch–Gordan coefficients and Eq. (41).

The above expressions can be used to evaluate all matrix elements of the irreducible spherical tensor operator directly from the elements of Grebenkov's $\mathcal{B}$ matrix. Once this is done, the components of the vector operator $\mathbf{A}$ are obtained via the relationships

$$X = \frac{1}{\sqrt{2}}(T_1^{-1} - T_1^{+1}), \tag{46a}$$

$$Y = \frac{i}{\sqrt{2}}(T_1^{-1} + T_1^{+1}), \tag{46b}$$

$$Z = T_1^0. \tag{46c}$$

IV. APPLICATION OF THE GENERALIZED MCF FRAMEWORK TO DOUBLE-PFG EXPERIMENTS

After the matrices Λ and $\mathbf{A}$ are evaluated for the particular geometry, the NMR signal attenuation can be written immediately. For example, in the case of the double-PFG experiment depicted in Fig. 1(b), it is given by

$$E = \langle 0|e^{-\Lambda\delta_1+i2\pi\mathbf{q}_1\cdot\mathbf{A}^\dagger}e^{-\Lambda(\Delta_1-\delta_1)} \times e^{-\Lambda\delta_1-i2\pi\mathbf{q}_1\cdot\mathbf{A}^\dagger}e^{-\Lambda(t_m-\delta_1)}e^{-\Lambda\delta_2-i2\pi\mathbf{q}_2\cdot\mathbf{A}^\dagger}e^{-\Lambda(\Delta_2-\delta_2)} \times e^{-\Lambda\delta_2+i2\pi\mathbf{q}_2\cdot\mathbf{A}^\dagger}|0\rangle^*. \tag{47}$$

Note that this expression holds for arbitrary parameters of this sequence. One variant of the double-PFG acquisitions is obtained when the second and third pulses, taken to be of equal duration ($\delta=\delta_1=\delta_2$), are applied simultaneously. In this case, the three exponentials in the middle are replaced by the single exponential $e^{-\Lambda\delta-i2\pi(\mathbf{q}_1+\mathbf{q}_2)\cdot\mathbf{A}^\dagger}$.

We performed simulations of the signal intensity for parallel plates as well as cylindrical and spherical pores. First, we performed simulations when the two gradients are parallel. The echo attenuation curves were found to be in agreement with those in Ref. 7 even when we changed the orientation of both gradients. To further test the dependence of the signal attenuation on the angle between the two gradients, we compared the results to those in Ref. 22, which were verified to be valid only in the low-q regime. Evidently, the application of the generalized MCF technique to double-PFG acquisitions provides a unified framework that is capable of modeling both the zero crossings of the diffraction experiments as well as the experiment's sensitivity on microscopic anisotropy.

In Fig. 2, we illustrate some simulation results for spherical pores. In Fig. 2(b), we show the NMR diffractograms where each curve represents a different value of the angle between the two gradients whose magnitudes are taken to be the same. Note that the positive sections of each curve are depicted using continuous lines whereas the negative sections are drawn with dotted lines. When the angle between the two gradients, denoted by ψ, is 0°, the second and third gradients of the double-PFG sequence of Fig. 1(b) are identical; this was the case considered in Ref. 7. On the other extreme, when ψ is 180°, the two center gradients are in opposite directions. Thus, for short values of the mixing time, the experiment resembles a single-PFG acquisition with a pulse separation of $2\Delta+t_m$, where $\Delta=\Delta_1=\Delta_2$. There-

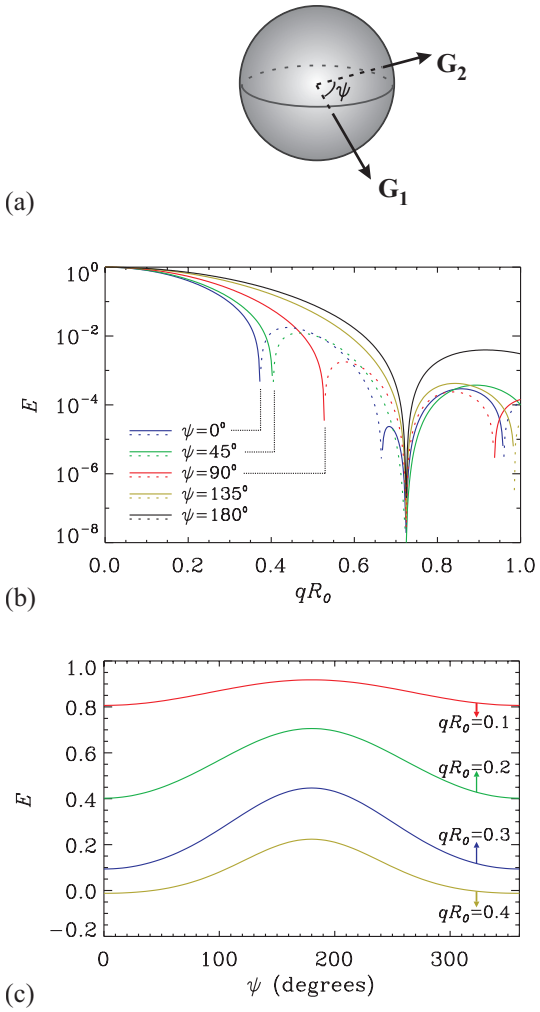

FIG. 2. (Color) (a) Spherical geometry and the two gradients of the double-PFG measurement considered. (b) Simulations of the double-PFG NMR signal for a sphere of radius R_0 as a function of the product of the q value with R_0. Different colors depict different angles between the two gradients (ψ). The portions of each curve depicted with continuous lines show the positive signal values, whereas the dotted lines depict the absolute value of the negative sections of each curve. (c) The NMR double-PFG signal plotted against the angle between the two gradient orientations for different gradient strengths. In both panels, the gradient strengths in the two PFG encodings of the experiment are taken to be the same. The other parameters are $R_0=5$ μm, $D_0=2\times10^{-3}$ mm^2/s, $\delta_1=\delta_2=0.04R_0^2/D_0$, $\Delta_1=\Delta_2=2R_0^2/D_0$, and $t_m=0.05R_0^2/D_0$.

fore, as expected, the zero crossings at half the q value disappear and one obtains the diffraction pattern characteristic of the single-PFG acquisitions[30] that does not exhibit any zero crossing, hence positive valued throughout. Note that the signal at $qR_0\simeq0.72$ vanishes for all values of ψ. This corresponds exactly to the qR_0 value at which single-PFG diffraction minimum is expected. As predicted in Ref. 7, this minimum is preserved in double-PFG acquisitions as well.

In Fig. 2(c), we show the effect of microscopic anisotropy by plotting the NMR signal attenuation against the angle ψ. This is the same problem addressed in Ref. 22. However, employing the generalized MCF approach enabled probing microscopic anisotropy at higher q values. Note that when $qR_0=0.4$ and when ψ is close to 0°, negative signal values are encountered as expected from Fig. 2(b).

A. Experiments on cylindrical microcapillaries

To provide experimental validation of the generalized MCF method, we performed experiments on a well characterized phantom consisting of water-filled microcapillaries with known inner diameters (IDs). We tested the dependence of the signal decay on the prolongation of the mixing time as well as the angle between the two gradients.

All measurements were performed in a Bruker 8.4 T NMR spectrometer capable of producing gradients of strength up to 190 G/cm along x, y, or z. The sequence was written in-house and calibrated as shown in Ref. 24. Hollow microcapillaries with nominal IDs of 10 ± 1 or 29 ± 1 μm (Polymicro Technologies, USA) were immersed in water for a period of several days prior to each experiment. The microcapillaries were packed into a 4 mm glass sleeve and then inserted into a 5 mm NMR tube which was aligned with the main axis of the microcapillaries parallel to the main magnetic field. Typical linewidths of 5–15 Hz were obtained after shimming. In all of the double-PFG experiments, the amplitudes of $\mathbf{G}_1$ and $\mathbf{G}_2$ were equal and stepped up in unison. The diffusion periods Δ were sufficiently long for the molecules to fully probe the boundaries. The echo times TE_1 and TE_2 (as defined in Ref. 24) were always chosen to be unequal to avoid overlapping echoes.

1. Dependence of the signal decay on the mixing time (t_m)

The sequence shown in Fig. 1(b) was used. Experiments were performed on microcapillaries with ID$=29\pm1$ μm. In these experiments, both of the gradients were kept in the x direction as illustrated in Fig. 3(a). Data at 24 q values were collected with $\delta_1=\delta_2=2$ ms, resulting in a maximal q value of 63.87 mm^{-1} ($G_{max}=75$ G/cm), $\Delta_1=\Delta_2=150$ ms, and the number of scans set to 128. Data at three different mixing times were collected: $t_m=6$, 30, and 100 ms.

Figure 3(b) shows the echo attenuation values for three different mixing times, plotted against the q value, which was the same in the two encodings of the double-PFG experiment. In such experiments, the signal can take negative values as originally predicted in Ref. 7 and experimentally observed in Ref. 24. As illustrated in Ref. 24, the experimental setup yielded robust information regarding the phase of the signal making it possible to recognize and distinguish the positive and negative data points. The curves, whose positive and negative sections are drawn with, respectively, continuous and dotted lines, are obtained by fitting the theoretical expression in Eq. (47) to real data whose positive and negative values are plotted using solid and hollow symbols, respectively. The agreement was very satisfactory. Slight deviations at high-q values were observed, most notably at the longest t_m. However, in the pulse sequence employed, the magnetization remained in the transverse plane during the t_m interval, hence suffering T_2 relaxation. Therefore this deviation can be attributed to noise. It should also be noted that the deviations on the right hand side are exaggerated in the log plot. The ID estimates for the diffraction experiments were 28.6, 28.7, and 29.1 μm, corresponding to the mixing times of 6, 30, and 100 ms, respectively. Compared with the

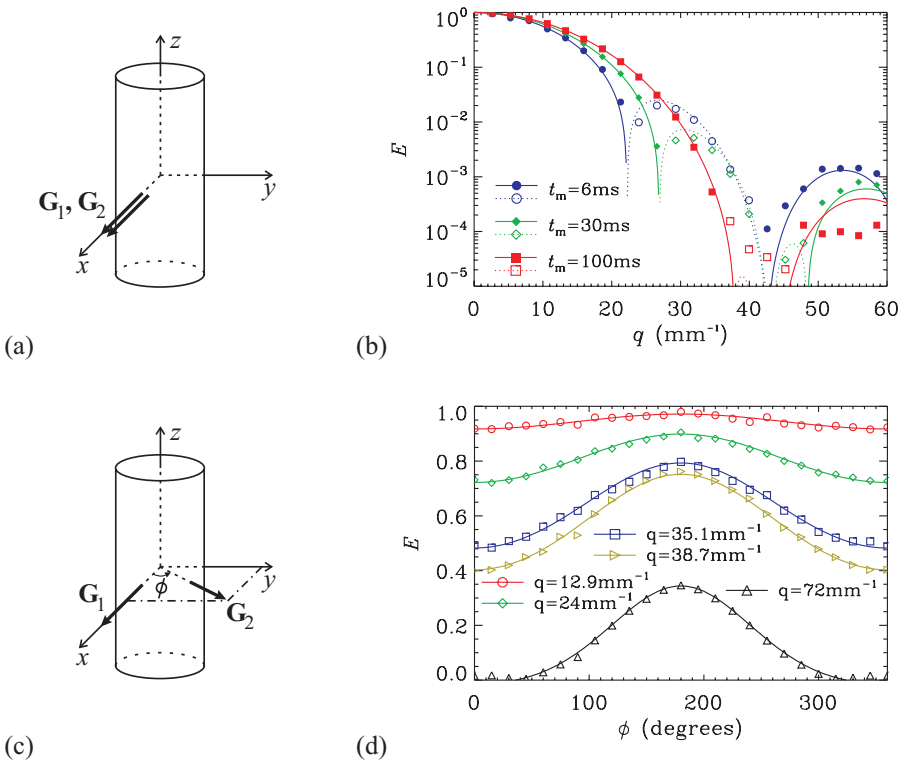

FIG. 3. (Color) (a) The cylindrical geometry and the gradient orientations employed in the double-PFG diffraction measurements. (b) Double-PFG diffraction data from cylindrical microcapillaries with nominal ID value of 29 ± 1 μm for three different values of the mixing time. In this panel, the continuous lines show the positive-valued sections of the simulation results whereas the dotted lines indicate the negative portions. Similarly, filled symbols depict the positive-valued experimental data points while the hollow symbols depict the negative-valued points. (c) The geometry and the gradient orientations for the angular double-PFG measurements. (d) Double-PFG NMR signal intensity plotted against the azimuthal angle (ϕ) of the second diffusion gradient. The experimental data points are shown with symbols, whereas the fitted curves are shown with continuous lines.

nominal diameter of 29 ± 1 μm, all of these estimates can be considered to be in agreement with the nominal IDs reported by the manufacturer.

2. Dependence of the signal decay on the azimuthal angle (ϕ)

A variant of the double-PFG sequence, obtained by simultaneously applying the second and third gradient pulses of Fig. 1(b) ($t_m=0$), was employed. For this set of experiments, microcapillaries with a nominal ID of 10 ± 1 μm were used. The first gradient was fixed along the x direction while the orientation of the second gradient was varied in the xy plane as illustrated in Fig. 3(c). Data at 25 values of ϕ were collected. The following parameters were used: Five q values were collected with $\delta_1=\delta_2=4.5$ ms, $\Delta_1=\Delta_2=40$ ms, and $G=6.73$, 12.53, 18.32, 20.20, and 37.57 G/cm, resulting in q values of 12.9, 24.0, 35.1, 38.7, and 72.0 mm^{-1}, respectively. The number of scans was set to 32. Due to a signal instability creating spurious fluctuations, for each of the smallest three q values, the signal values at $\phi=135°$ and $\phi=225°$ were replaced with the average of the two signal values at the neighboring angles.

In Fig. 3(d), we show the dependence of the NMR signal attenuation on the angle between the two gradients, both of which had the same magnitude. The data points are depicted with symbols. A curve was fitted to the data at each q value separately. The ID estimates for the angular dependence experiments were 10.0, 10.3, 10.3, 10.4, and 10.4 μm, corresponding to q values of 12.9, 24.0, 35.1, 38.7, and 72.0 mm^{-1}, respectively. These values are in agreement with the manufacturer's nominal value of 10 ± 1 μm.

V. DISCUSSION AND CONCLUSION

In this article, we presented a generalization of the MCF approach that enabled the estimation of the NMR signal intensity from general gradient waveforms even when the gradient orientation is changed during the acquisition. This was possible by utilizing conceptually sophisticated analytical machinery that is employed routinely in quantum mechanics. The operator algebra and the Wigner–Eckart theorem yielded the relevant matrix elements without the need to evaluate complicated integrals.

In the above treatment, we did not tackle the issue of surface relaxation explicitly. In a recent article,[31] Grebenkov showed a way to conveniently incorporate the effects of surface relaxation into the MCF framework by introducing another scalar operator. It is clear from the above theoretical treatment that scalar operators (e.g., the Λ operator) are invariant when the direction of the gradients is changed. Therefore, the matrix elements of the surface relaxation operator do not need to be updated for general gradient waveforms.

When one moves from MCF to its generalized version, incorporating the effects of variations in the gradient orientation for the cylindrical pore does not increase the computational burden of the MCF method other than by a simple matrix addition. Contrary to the case of cylinders, the generalization for spherical pores necessitates matrices of larger dimension to be employed. This is because the new matrices have an additional index, m. Therefore, each matrix element in Ref. 18 has to be replicated $2l+1$ times since m values vary between $-l$ and l. For example, if we keep the first ten eigenvalues according to the description in Ref. 18, the matrices we have to construct are 46×46. Similarly, the first 20 eigenvalues require 146×146 matrices. This suggests that there is a limit to the accuracy that can be obtained when the

generalization of the MCF framework is employed for spherical pores. However, no apparent deviation from the expected behavior was encountered in our simulations that employed 20 eigenvalues.

The biggest advantage of the present method over the previously introduced multiple propagator approach, which also utilizes matrix operators,[4] is that it is possible to write the results analytically for piecewise-constant gradient waveforms in a straightforward manner. As was shown in Ref. 22 the multiple propagator approach can be envisioned to be a path integral method, according to which taking the limit of the signal as the duration of the intervals tends to 0 enables one to obtain an analytical result. Although it was possible to evaluate the quadratic term of the signal analytically in Ref. 22, it proved difficult to apply the same approach to obtain the higher order terms in a Taylor series representation of the NMR signal decay. Moreover, from a practical point of view, in the multiple propagator approach, one has to introduce a temporal grid on top of the gradient waveform. This is an artificial construct unless the gradient waveform is composed of true delta functions, and the interval between the consecutive impulses in this artificial grid influences the end result. In the MCF approach, however, there is no need for such "time slicing" for piecewise gradient waveforms; the start and end points of each pulse naturally introduce an appropriate scheme for time sampling. Finally, in our experience, we observed the MCF approach to be significantly more efficient from a computational standpoint.

It should be noted that although we considered only very simple geometries of cylinders and spheres in the formulations, many media of interest exhibit different types of complexity. For example, in most biological tissues and emulsions, the compartments can be assumed to possess differing degrees of dimensional and orientational heterogeneities. The theory developed here can be generalized in a straightforward way to account for such variations as was done in Ref. 22.

In an earlier publication, anisotropy induced by restricting boundaries was exploited to map the directions normal to macroscopic interfaces[32] using single-PFG image acquisitions, which was possible due to the edge enhancement mechanism.[33] It was demonstrated that the anisotropy observed in double-PFG experiments with short mixing times can be attributed to the same kind of anisotropy, this time in microscopic pores.[22] In this work, mapping of microscopic anisotropy was generalized to data obtained with higher $2\pi qa$ values, where a is a characteristic pore dimension. This is important because *a priori* knowledge of the pore dimension is usually not available; thus it may be difficult to satisfy this condition and simultaneously achieve observable levels of signal attenuation. This is a particularly important concern in imaging studies where pore size is expected to vary from region to region and in examining heterogeneous specimens characterized by a distribution of pore sizes. Using the generalization of the MCF framework, it is possible to observe microscopic anisotropy using completely arbitrary experimental parameters.

ACKNOWLEDGMENTS

This research was supported by the Intramural Research Program of the Eunice Kennedy Shriver National Institute of Child Health and Human Development, National Institutes of Health (NIH).

[1] E. L. Hahn, Phys. Rev. **80**, 580 (1950).
[2] E. O. Stejskal and J. E. Tanner, J. Chem. Phys. **42**, 288 (1965).
[3] A. Caprihan, L. Z. Wang, and E. Fukushima, J. Magn. Reson., Ser. A **118**, 94 (1996).
[4] P. T. Callaghan, J. Magn. Reson. **129**, 74 (1997).
[5] S. L. Codd and P. T. Callaghan, J. Magn. Reson. **137**, 358 (1999).
[6] A. L. Sukstanskii and D. A. Yablonskiy, J. Magn. Reson. **157**, 92 (2002).
[7] E. Özarslan and P. J. Basser, J. Magn. Reson. **188**, 285 (2007).
[8] L. Avram, E. Özarslan, Y. Assaf, A. Bar-Shir, Y. Cohen, and P. J. Basser, NMR Biomed. **21**, 888 (2008).
[9] A. Bar-Shir, L. Avram, E. Özarslan, P. J. Basser, and Y. Cohen, J. Magn. Reson. **194**, 230 (2008).
[10] A. V. Barzykin, Phys. Rev. B **58**, 14171 (1998).
[11] A. V. Barzykin, J. Magn. Reson. **139**, 342 (1999).
[12] H. Y. Carr and E. M. Purcell, Phys. Rev. **94**, 630 (1954).
[13] B. Robertson, Phys. Rev. **151**, 273 (1966).
[14] S. Meiboom and D. Gill, Rev. Sci. Instrum. **29**, 688 (1958).
[15] P. N. Sen, A. André, and S. Axelrod, J. Chem. Phys. **111**, 6548 (1999).
[16] S. Axelrod and P. N. Sen, J. Chem. Phys. **114**, 6878 (2001).
[17] D. S. Grebenkov, Rev. Mod. Phys. **79**, 1077 (2007).
[18] D. S. Grebenkov, Concepts Magn. Reson. **32A**, 277 (2008).
[19] D. S. Grebenkov, J. Chem. Phys. **128**, 134702 (2008).
[20] D. G. Cory, A. N. Garroway, and J. B. Miller, Polym. Prepr. (Am. Chem. Soc. Div. Polym. Chem.) **31**, 149 (1990).
[21] P. P. Mitra, Phys. Rev. B **51**, 15074 (1995).
[22] E. Özarslan and P. J. Basser, J. Chem. Phys. **128**, 154511 (2008).
[23] N. Shemesh, E. Özarslan, P. J. Basser, and Y. Cohen, "Measuring small compartmental dimensions with low-q angular double-PGSE NMR: The effect of experimental parameters on signal decay," J. Magn. Reson., DOI:10.1016/j.jmr.2009.01.004 (in press).
[24] N. Shemesh and Y. Cohen, J. Magn. Reson. **195**, 153 (2008).
[25] H. C. Torrey, Phys. Rev. **104**, 563 (1956).
[26] S. Ryu, Magn. Reson. Imaging **19**, 411 (2001).
[27] K. R. Brownstein and C. E. Tarr, Phys. Rev. A **19**, 2446 (1979).
[28] P. T. Callaghan, *Principles of Nuclear Magnetic Resonance Microscopy* (Clarendon, Oxford, 1991).
[29] E. Merzbacher, *Quantum Mechanics* (Wiley, New York, 1998).
[30] P. T. Callaghan, A. Coy, D. MacGowan, K. J. Packer, and F. O. Zelaya, Nature (London) **351**, 467 (1991).
[31] D. S. Grebenkov, Phys. Rev. E **76**, 041139 (2007).
[32] E. Özarslan, U. Nevo, and P. J. Basser, Biophys. J. **94**, 2809 (2008).
[33] W. B. Hyslop and P. C. Lauterbur, J. Magn. Reson. **94**, 501 (1991).